Lawrence Berkeley National Laboratory

Title
Residual strain orientation in rolled titanium determined with synchrotron X-ray Laue microdiffraction

Permalink
https://escholarship.org/uc/item/7r14v174

Journal
Journal of Applied Crystallography, 56(Pt 1)

ISSN
0021-8898

Authors
Devoe, Michelle
Tamura, Nobumichi
Wenk, Hans-Rudolf

Publication Date
2023-02-01

DOI
10.1107/s1600576722011311

Copyright Information

Peer reviewed

Residual strain orientation in rolled titanium determined with synchrotron X-ray Laue microdiffraction

Authors

XMichelle Devoe[a]*, Nobumichi Tamura[b] and Hans-Rudolf Wenk[a]

[a]Earth and Planetary Science, University of California, Berkeley, CA, 94720, United States

[b]Advanced Light Source, Lawrence Berkeley National Laboratory, Berkeley, CA, 94720, United States

Correspondence email: mdevoe@berkeley.edu

ynopsis   Synchrotron X-ray Laue microdiffraction is used to measure the residual stress in rolled titanium, a metal with known deformation history, and determine the orientation of the residual stress ellipsoid. Previously the method had only been used on naturally deformed quartzites with ambiguous deformation histories.

bstract   Previously, synchrotron X-ray Laue microdiffraction has been used to measure magnitudes of residual strain in materials. Recently the method was advanced to determine the orientation of the strain ellipsoid and applied to naturally deformed quartzites, however the deformation history of these quartzites is ambiguous due to their natural origin. In this study, synchrotron X-ray Laue microdiffraction (µXRD) is used to measure the residual strain for the first time in a sample with known stress history, rolled titanium. A deviatoric strain tensor is calculated from each Laue diffraction image collected with two µXRD scans of a rolled Ti sheet in different sample orientations. The principal strain axes are calculated using an eigen decomposition of the deviatoric strain tensors. The results show that the principal axis of compression is aligned with the normal direction of the titanium sheet, and the principal axis of extension is aligned with the rolling direction. Pole figures are used to represent the 3D distribution of residual strain axes.

eywords: Residual stress; residual strains; stress and strain; X-ray synchrotron radiation; Laue diffraction

33

1. Introduction

Residual stress has been of interest to metallurgists and structural engineers for decades (e.g. Noyan & Cohen, 1987). It affects the strength of metals and welds and is significant for the stability of ships, pipelines, bridges (e.g. Hosford, 2005; Withers, 2005; Van Puymbroeck et al., 2019), and the strength of thin films (e.g. Noyan et al., 1995; Ma et al., 2012). Residual stress can be introduced into a material at any point during fabrication and processing from mechanical working or heat treatment, and thus its characterization is key to understanding not only the quality of the material, but also the effects of the manufacturing process on material properties.

Residual strain is a change to the lattice geometry of a crystalline material as a result of deformation or thermal changes. Residual strain, which remains in the lattice after the external forcing has been removed, can be categorized as plastic strain, which manifests as dislocations that disrupt the periodicity of the crystalline lattice, or elastic strain, which describes the shape distortion of the crystal lattice surrounding dislocations (Noyan & Cohen, 1987). These strains are related to stress through Hooke's law. Many techniques have been developed to detect and measure strain in metals (e.g. Schajer, 2013). Bulk properties can be measured with neutron diffraction due to its great penetration depth (Krawitz & Holden, 1990; Robinson et al., 2017; Noyan et al. 2020; Wissink et al., 2020). X-ray diffraction (XRD) has been used as a non-destructive method (Ungár & Borbély, 1996; Ungár et al., 2001; Cauchois et al., 2014). Single crystal properties can be measured using synchrotron X-ray microdiffraction (μXRD) (Tamura et al., 2002; Levine et al., 2006; Renversade & Borbély, 2017; Morawiec, 2018). μXRD utilizes a micro-focused polychromatic X-ray beam from a synchrotron X-ray source with a diameter of ~0.1-1 μm to raster scan a crystalline material over a large area (mm) and collects 2D Laue images at each step. The subsequent analysis generates high-resolution strain maps of polycrystalline materials (Spolenak et al., 2003; Ice et al., 2005; Hofmann et al., 2010; Kwon et al., 2013; Jiang et al., 2014; Qian et al., 2017). If the grain size is larger than the beam diameter and step size, strain differentials may be resolved across grain boundaries (Spolenak et al., 2003).

For the past 10 years, we have analyzed the orientation of macrostresses responsible for residual strain in natural quartzite using μXRD and have found results consistent with the stress history presumed from geological events. We developed a methodology to represent the 3D orientation of residual strain axes with pole figures generally used for crystal orientations or textures (Chen et al., 2011; Chen et al., 2016; Li et al. 2020; Wenk et al., 2020). However, the stress history of geological materials is complex, enduring a variety of stresses over long time scales, and thus there remains some uncertainty about their presumed stress history. Therefore, we decided to test μXRD

67   and our experimental and analytical approach on a simple metal with a known deformation history to

68   verify the accuracy of the results.

69   Studies looking at directionality of residual strain in metals have been primarily focused on

70   cubic metals (Spolenak et al., 2003; Shen et al., 2022 *in press*). In this study, we determine the

71   directionality of the residual strain tensor of a hexagonal metal, titanium, with µXRD. The strength,

72   corrosion resistance, and other mechanical and chemical properties of Ti and its alloys make them

73   useful in a number of engineering sectors, including aerospace, nuclear, automotive, and

74   bioengineering (e.g. Lütjering et al., 2007; Mehta et al., 2007; Wang et al., 2020) and the

75   microstructures and textures of Ti and Ti alloys have been well-characterized (Patridge, 1967;

76   Blicharski et al., 1979; Zaefferer, 2003; Lonardelli et al., 2007; Britton et al., 2015; Guo et al., 2015).

77   We present strain maps and 3D orientation distributions of the residual strain tensor, equivalent stress

78   calculations, and the deformation texture of rolled Ti derived from µXRD data.

79   **2. Experimental Methodology**

80   A 1.2 mm thick sheet of ASTM B 295 Grade 4 commercially pure rolled Ti was cut into a 1.8 x 1.4

81   cm piece used for analysis. The sample grain size ranges from 5 to 30 µm. Grains appear to be

82   flattened with a long axis parallel to the rolling direction (RD) (Fig. 1).
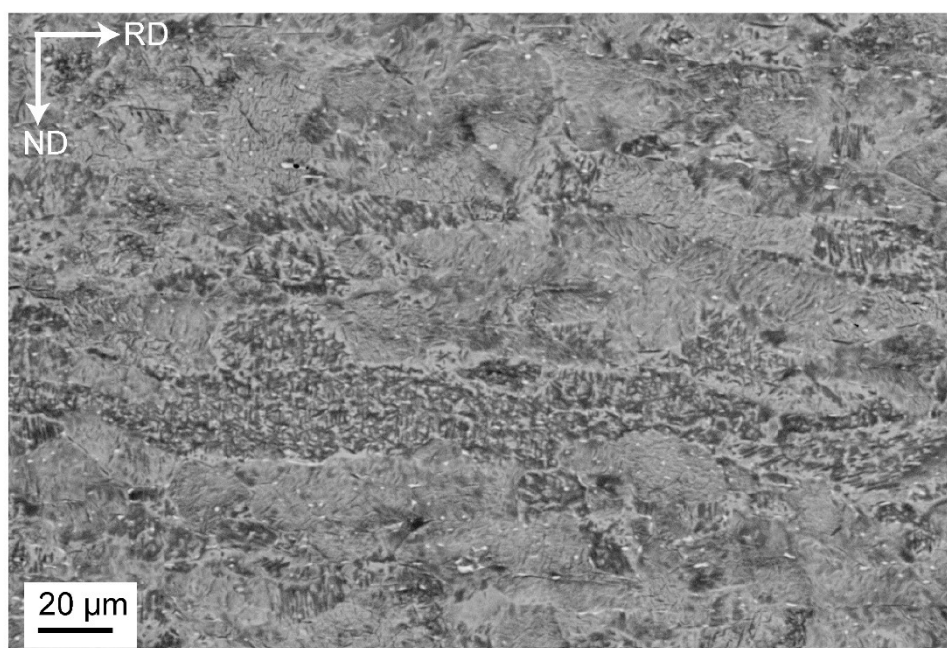
83

84   **Figure 1**   Scanning electron microscope backscatter electron image of cross section of rolled

85   titanium. RD is rolling direction, ND is normal direction.

86

87   **2.1. X-ray Laue Microdiffraction**

88   X-ray Laue microdiffraction (µXRD) measurements were conducted at beamline 12.3.2 of the

89   Advanced Light Source at Lawrence Berkeley National Laboratory. The methodology has been

90   previously described (Tamura, 2014; Chen et al., 2016; Li et al., 2020; Wenk et al., 2020). The 1.8 x

91   1.4 x 0.12 mm Ti sample was loaded onto a translational stage. The stage was tilted 45° to the

92   incident X-ray beam (Fig. 2A). A polychromatic X-ray beam with energy range of 5 to 24 keV was

93   collimated to a spot size 1 µm in diameter. The rolled surface, perpendicular to the normal direction

94   (ND), of the Ti sample was placed at the focal point of the X-ray beam using a laser proxy. The

95   translational stage then rastered across the X-ray beam at the user-set step size and scan dimensions

96   which are programmed using the beamline control software. 2D diffraction images (Fig. 2B) were

97   collected at each step by a DECTRIS Pilatus 1M detector positioned 90° to the incident beam.

98   Maximum penetration depth is 100 µm (source: CXRO.lbl.gov).
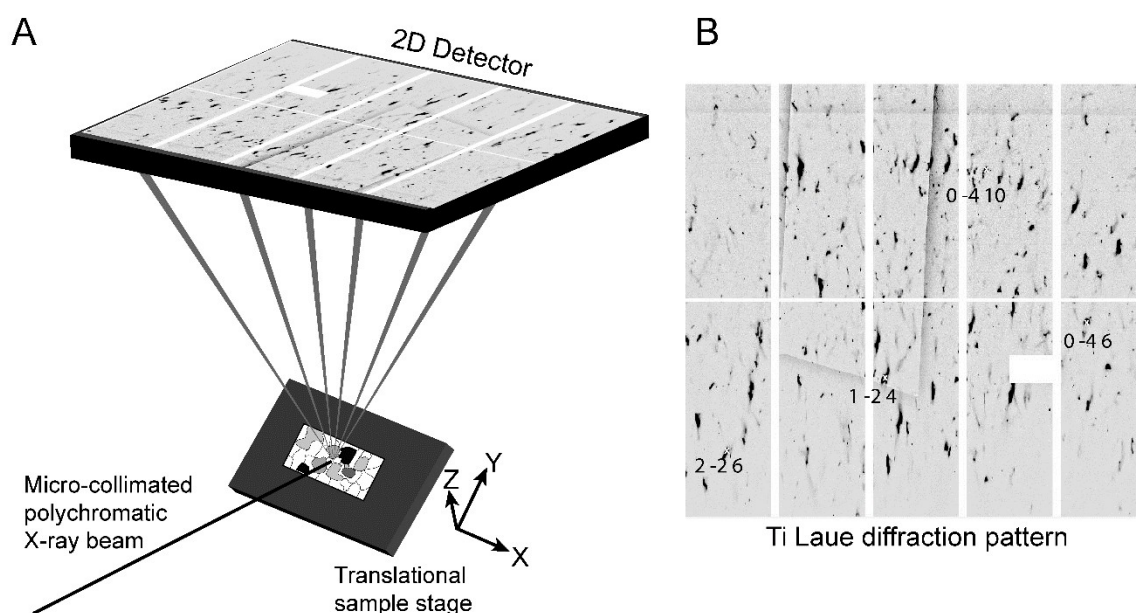
100   **Figure 1**   A) Schematic of beamline experimental geometry at ALS 12.3.2 showing polycrystalline

101   Ti sample on translational stage.- DECTRIS Pilatus 1M Area detector located 90° above the incident

102   X-ray beam collects a diffraction image. B) Example Ti X-ray Laue diffraction image. A few

103   exemplary peaks have been assigned Miller indices. White lines are interstitial space between detector

104   panels. White rectangle in bottom right is a defective submodule that has been removed from

105   analysis.- Dark vertical shadow is the boundary of Kapton tape used to repair the detector.

106

107   A single crystal of silicon crushed into grains ranging in size from 0.05 to 2 mm were

108   mounted on a glass slide with double-sided sticky tape and used as a calibrant. This is different from

109   previous experiments which used a single crystal of silicon or synthetic quartz (Chen et al., 2016;

110   Wenk et al., 2020). The multiple peaks generated from a polycrystalline calibrant (Fig. 3A) eliminate

111   the orientation bias that is introduced into the strain analysis from the use of a single crystal calibrant,

112   which only has a few peaks on each detector panel (Fig. 3B). The calibration is used in data

113   processing and does not affect the data collection.

114   An area of 1500 x 2000 μm on the rolled surface of the Ti sample was scanned with the X-ray

115   beam in 50 μm steps to cover a large area for good grain statistics (scan Ti_6). While a 1 um step size

116   is achievable at beamline ALS 12.3.2, the grain size of the sample ranged from 5 to 30 um and thus

117   use of a 1 um step size would sample a very limited number of grains during a reasonable collection

118   time period. Thus, a larger step size of 50 um was chosen to measure a large number of grains and

119   collect data more representative of the whole sample. Exposure time was 1 s and the scan took

120   approximately 20 mins to complete. Since the maximum penetration depth of X-rays is 100 um,

121   approximately 1/12 of the depth profile of the rolled Ti sheet was sampled. The sample was then

122   rotated 90° and approximately the same area was re-scanned (scan Ti_6_90d). The purpose of this

123   repeated scan is to verify that the orientation of residual strain rotates with sample rotation,

124   demonstrating that the strain measured is not an artifact due to calibration geometry uncertainties and

125   other errors.
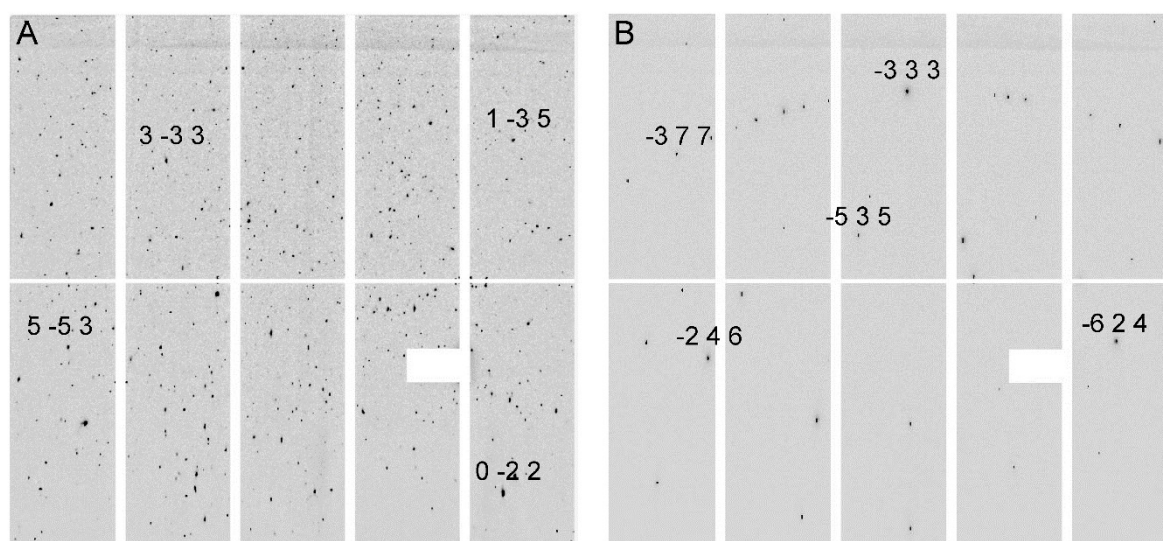
127   **Figure 2**   X-ray Laue diffraction images of A) polysilicon calibrant and B) single crystal silicon

128   calibrant. A few exemplary peaks have been assigned Miller indices. White lines are interstitial space

129   between detector panels. White rectangle is a defective submodule that has been removed from

130   analysis.

131   **1.1. Data Analysis Overview**

132   A more detailed explanation on data analysis has been published by Tamura (2014) and Wenk et al.

133   (2020). The total strain tensor (ε_{ij}) is a sum of the dilatational strain tensor (Δ_{ij}), which describes a

134   change in volume of the unit cell, and the deviatoric strain tensor (ε_{ij}'), which describes a change in

135   shape (Fig. 4A): $\varepsilon_{ij} = \Delta_{ij} + \varepsilon_{ij}'$

136   where $\Delta_{ij} = \begin{bmatrix} \delta & 0 & 0 \\ 0 & \delta & 0 \\ 0 & 0 & \delta \end{bmatrix}$

137   and $\varepsilon_{ij}' = \begin{bmatrix} \varepsilon_{11}' & \varepsilon_{12} & \varepsilon_{13} \\ \varepsilon_{12} & \varepsilon_{22}' & \varepsilon_{23} \\ \varepsilon_{13} & \varepsilon_{23} & \varepsilon_{33}' \end{bmatrix}$

138   In our analysis, the deviatoric strain tensor is first transformed from the coordinate system of the

139   diffraction image, a Cartesian coordinate system attached to the unit cell, to the sample coordinate

140   system (x, y, z) using the orientation matrix M and transformation $\varepsilon_{xyz}' = M \varepsilon_{ij}' M^T$. Such that

141         $\varepsilon_{xyz}' = \begin{bmatrix} \varepsilon_{xx}' & \varepsilon_{xy} & \varepsilon_{xz} \\ \varepsilon_{yx}' & \varepsilon_{yy}' & \varepsilon_{zz} \\ \varepsilon_{zx} & \varepsilon_{zy} & \varepsilon_{zz}' \end{bmatrix}$

142   An eigen decomposition of ε_{xyz}' provides the geometry of the deviatoric strain ellipsoid in sample

143   coordinates; the eigenvectors are the axes of the ellipsoid scaled by their associated eigenvalues (Fig.

144   4B) (Noyan & Cohen, 1987; Tamura, 2014). Negative values are herein defined as compression, and

145   positive values are defined as extension.
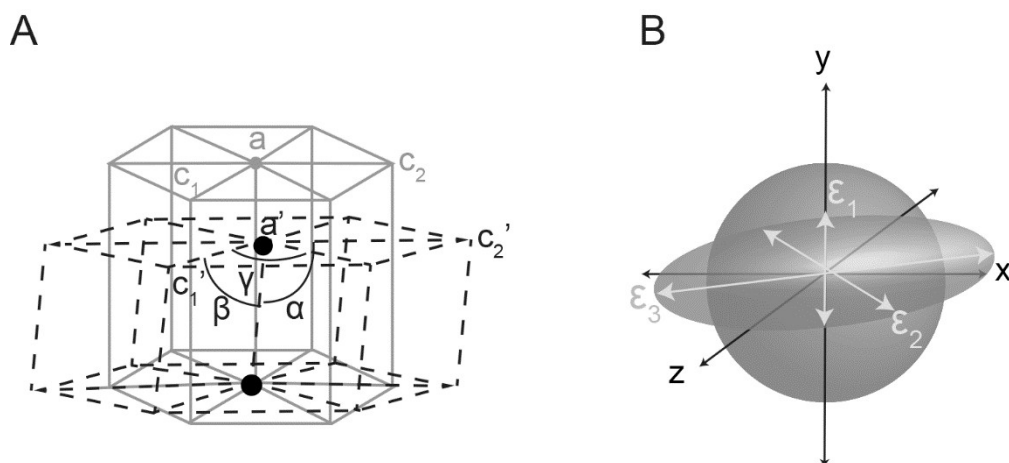
146

147   **Figure 3**   A) Hexagonal unit cell (solid lines, lattice parameters a, c_1, c_2) distorted into a new triclinic

148   shape (dashed lines, lattice parameters a', c_1', c_2', α, β, γ). B) A sphere (light gray) is distorted into a

149   strain ellipsoid (yellow) to represent the distortion shown in (A). Strain ellipsoid axes (ε_1, ε_2, ε_3) are

150   noted relative to sample coordinate axes (x, y, z).

151   **1.2. How deviatoric strain is measured and principal stress is calculated**

152   The XMAS software determines the crystal orientation and calculates the deviatoric strain tensor for

153   each diffraction image. In this experiment, 1,200 diffraction images were collected for each scan. The

154   experimental geometry was refined using the polysilicon calibrant (Fig. 3A). The strain is refined

155   from the lattice parameters of the deformed crystal relative to those of unstrained Ti (Fig. 4A). The

156   diffraction images are preprocessed by removing bad pixels and background signal due to air

157   scattering and X-ray fluorescence. Next, the reflection positions are located by finding intensity

158   maxima above a certain threshold value, and peaks are fit with a 2D Gaussian function. Then, each

159   peak is "indexed" and assigned a corresponding *hkl* plane by triangulation of three peak positions.

160   The crystal orientation can then be derived from the indexation.

161   The deviatoric strain is calculated by measuring the difference between the observed position

162   of the measured diffraction peaks and the ideal position of peaks calculated for an unstrained lattice.

163   XMAS searches for three unique grain orientations per diffraction image using the "multigrain"

164   setting. If a diffraction image cannot be indexed by XMAS, the grain orientation and strain tensor

165   cannot be calculated and is thus excluded from the analysis. After the indexation parameters of a

166   representative Laue image have been optimized for accurate analysis, the rest of the Laue images are

167   automatically processed using the same parameters on a high-performance computing cluster.

168   The output from XMAS, a sequential list file which contains the crystal orientations and strain

169   tensor for every diffraction image indexed, is then loaded into the MATLAB code XtalCAMP (Li et

170   al., 2020). Orientation and magnitude of the principal strain axes are calculated for each diffraction

171   image using an eigen decomposition of the deviatoric strain tensor. Strain maps and other

172   visualizations are also plotted using this software. Stress (σ_{ij}) can be calculated from strain (ε_{kl}) by

173   applying Hooke's law: $\sigma_{ij} = C_{ijkl}\,\varepsilon_{kl}$ where C_{ijkl} is the fourth rank stiffness tensor. We used the

174   experimental stiffness tensor components of monocrystal hcp-Ti determined by Dumontet et al.

175   (2019). Prior to plotting the strain maps and calculating the principal strains, all diffraction images

176   with less than 10 indexed reflections were filtered out to eliminate strain measurements with low

177   confidence. Low indexation is likely due to peak distortion from high strain. After filtering, the

178   deviatoric and principal strains were calculated for each diffraction image and the strain maps of the

179   scan area were generated (Figs. 5 & 6). Normalized frequency distributions of equivalent strain and

180   stress were also plotted for each scan using XtalCAMP (Fig. 7).

181   From XtalCAMP the orientations of the crystal and the residual strain ellipsoid for each

182   diffraction image, defined by three Euler angles relative to sample coordinates, were then exported

183   and used by BEARTEX (Wenk et al., 1998) to generate 3D orientation distributions and plot

184   corresponding pole figures (Figs. 8 and 9).

185   **Fig**

186
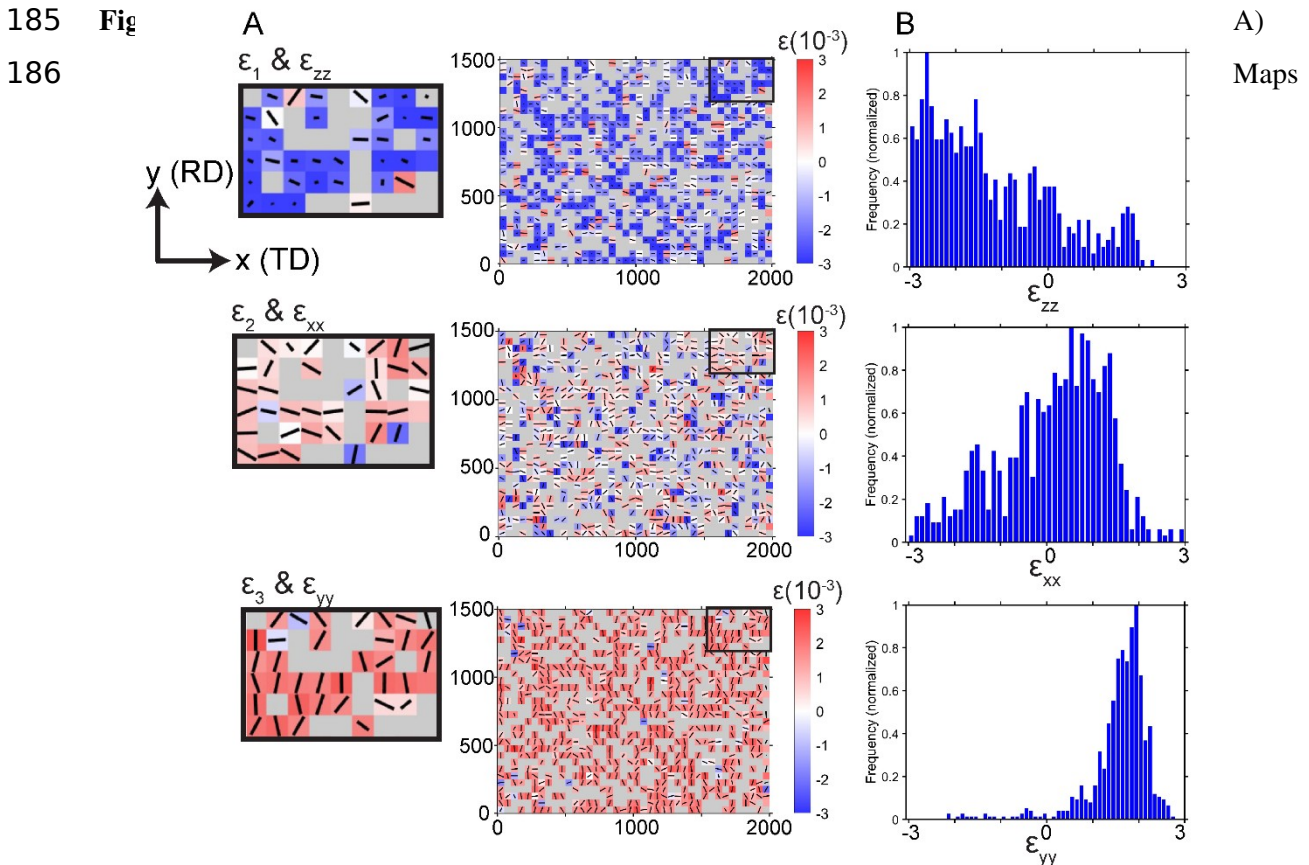
187   showing the magnitude of the $\varepsilon_{xx}, \varepsilon_{yy}, \varepsilon_{zz}$ components of the deviatoric residual strain tensor in sample

188   coordinates (x, y) for Ti_6 scan of dimensions 2000 x 1500 mm with step size of 50 μm. Projections

189   of principal strain axes ε_1, ε_2, or ε_3 are overlain onto each pixel as a black line (enlarged inset on left).

190   Each pixel represents one step and shows the data associated with the diffraction image collected at

191   that step. The color of each pixel indicates the deviatoric strain magnitude at that position in

192   millistrains (10^{-3}). Red color (positive values) indicates extension, blue color (negative values)

193   indicates compression. Gray pixels are Laue diffraction images that had less than 10 indexed

194   reflections and were thus removed from analysis. RD is rolling direction, TD is transverse direction.

195   B) Normalized frequency distributions of residual strain values from plots in (A).
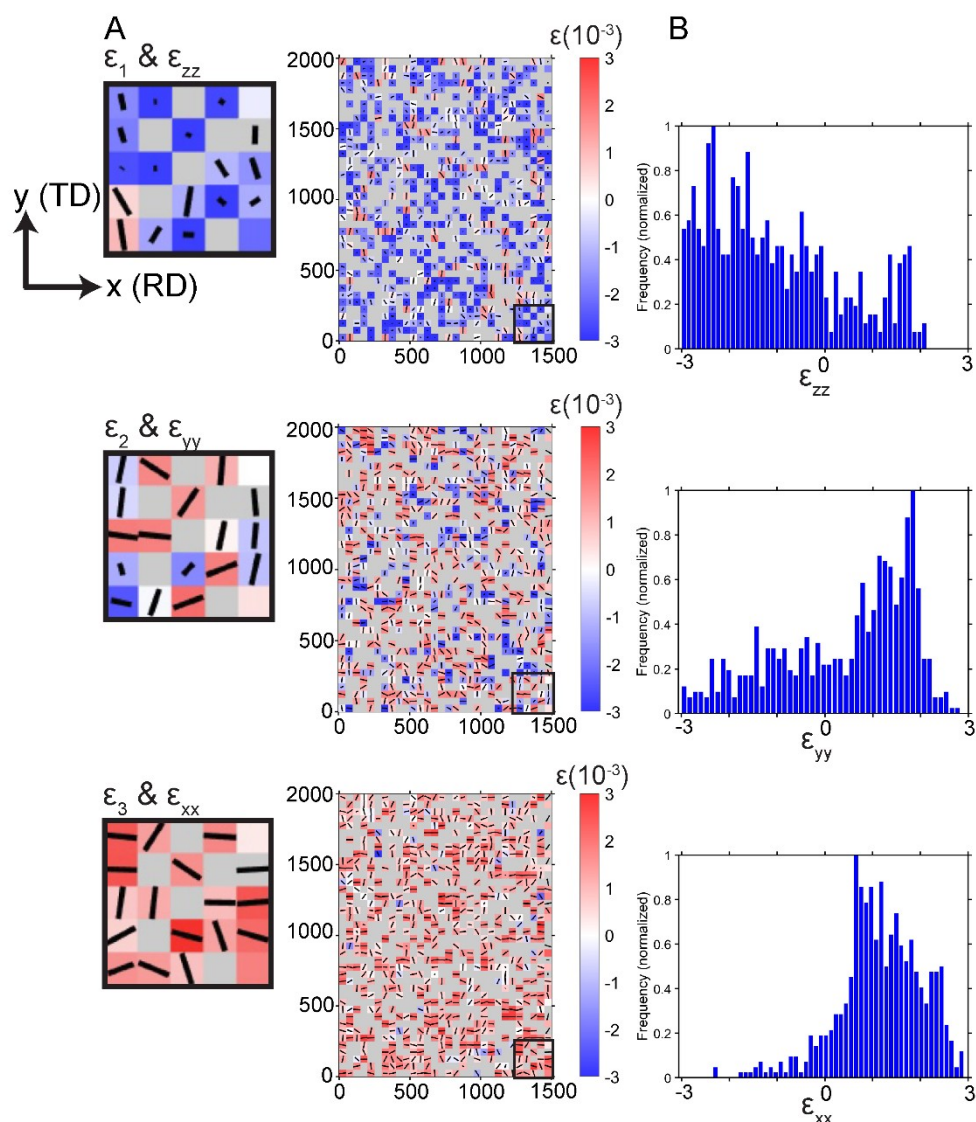
Figure 5 A) Maps showing the magnitude of the ε_{xx}, ε_{yy}, ε_{zz} components of the deviatoric residual strain tensor in sample coordinates (x, y) for Ti_6_90d scan of dimensions 1500 x 2000 mm with step size of 50 μm. Projections of principal strain axes ε_1, ε_2, or ε_3 are overlain onto each pixel as a black line (enlarged inset on left). Each pixel represents one step and shows the data associated with the diffraction image collected at that step. The color of each pixel indicates the deviatoric strain magnitude at that position in millistrains (10^{-3}). Red color (positive values) indicates extension, blue color (negative values) indicates compression. Gray pixels are Laue diffraction images that had less than 10 indexed reflections and were thus removed from analysis. RD is rolling direction, TD is transverse direction. B) Normalized frequency distributions of residual strain values from plots in (A).
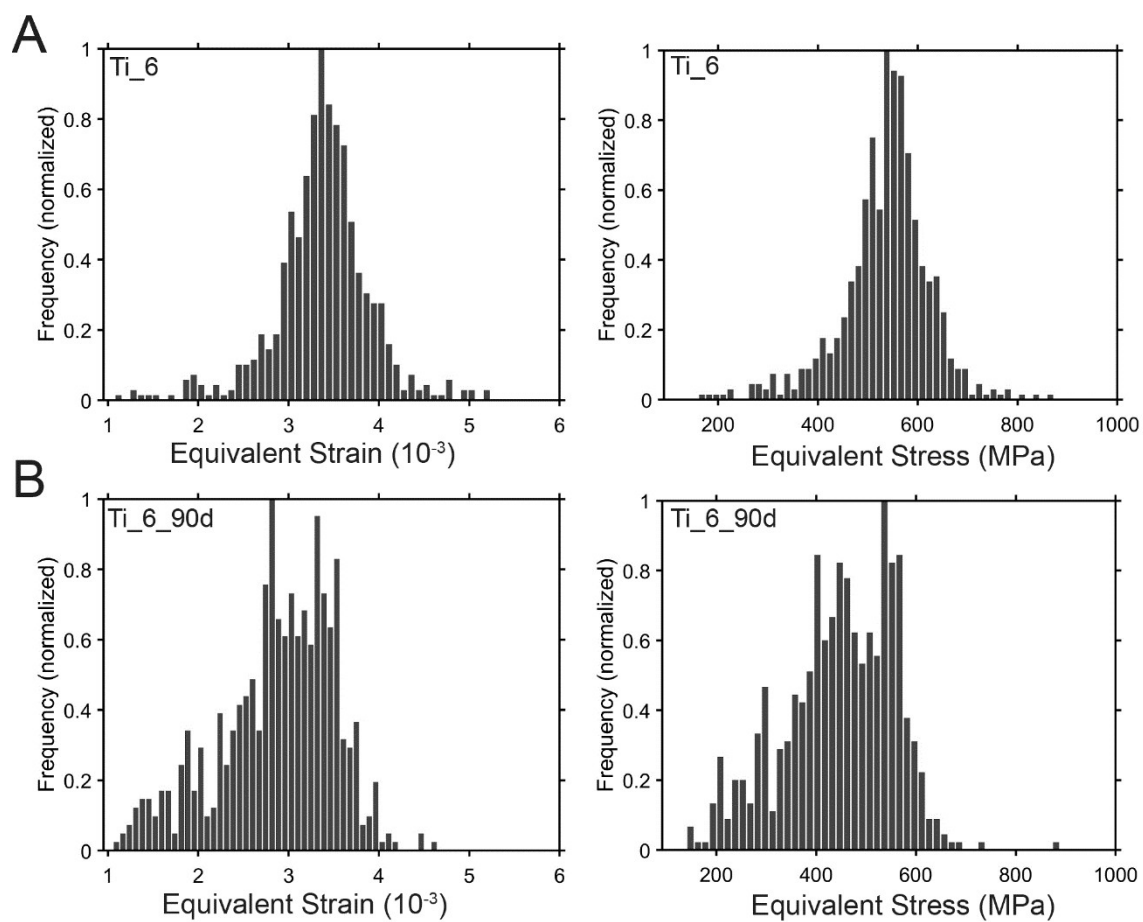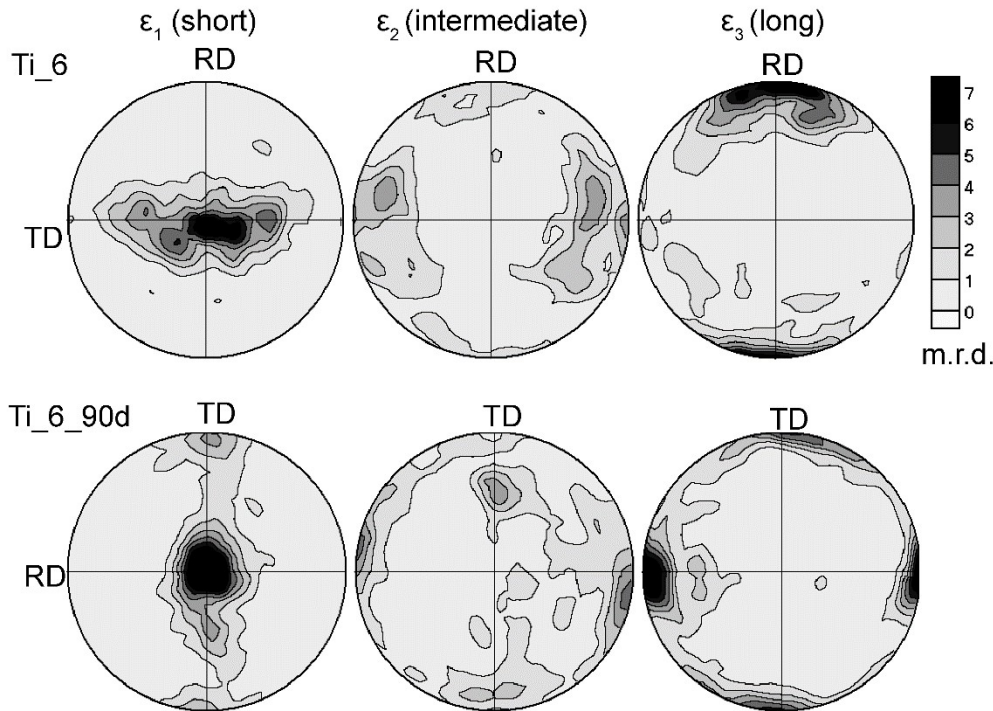
**Figure 6** Normalized equivalent strain and stress distributions for Ti_6 (A) and Ti_6_90d (B).

Figure 7 Principal strain axes for Ti_6 (top) and Ti_6_90d (bottom) plotted as pole figures in equal area projection. Pole figures provide a 3D representation of the principal axes of compression (ε_1), intermediate strain ($\varepsilon2$) and extension (ε_3) relative to sample coordinates. RD is rolling direction, TD is transverse direction. Contours are in multiples of random distribution (m.r.d.).
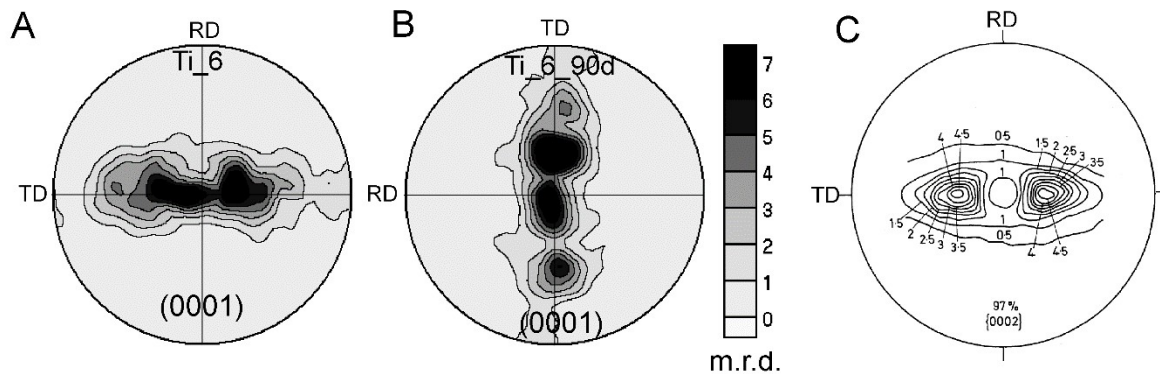
Figure 8 Deformation textures of crystal (0001) poles plotted as equal area projection pole figures for Ti_6 (A) and Ti_6_90d (B). RD is rolling direction, TD is transverse direction. Contours are in multiples of random distribution (m.r.d.). C) Equal area projection of deformation texture for (0002) poles for rolled Ti reduced to 3% of its original thickness measured with an X-ray pole figure goniometer (Blicharski et al., 1979).

223   **2. Results**

224   The μXRD data are most easily understood visually using maps to spatially resolve the data collected

225   from the scanned area. Because grain size of the sample ranged from 5 to 30 μm in diameter (Fig. 1),

226   and the beam raster step for each scan was 50 μm, grains cannot be resolved in the maps generated

227   (Figs. 5 & 6). Pole figures of strain ellipsoid axes (i.e. principal strain axes) are used to compile the

228   data into a 3D representation of residual strain orientation in sample coordinates (Fig. 8).

229   **2.1. Strain**

230   Strain maps for each scan are plotted in Figures 5 (Ti_6) and 6 (Ti_6_90d). Three maps are displayed

231   for each scan, one for each deviatoric strain component (ε_{xx}, ε_{yy}, and ε_{zz}) (Figs. 5A, 6A). ε_{xx} is

232   deviatoric strain along the x-axis, ε_{yy} along the y-axis, and ε_{zz} along the z-axis. The color of each pixel

233   corresponds to the magnitude of the deviatoric strain component; red indicates positive strain

234   (extension) and blue indicates negative strain (compression). Deviatoric strain values range from -3 to

235   3 millistrains (10^{-3}). The frequency distributions (Figs. 5B, 6B) of the deviatoric strain magnitudes

236   clearly indicate the direction of the most compressive (negative), and most tensile (positive) strain.

237   Strains are most negative in the direction normal to the sample surface (z=ND) for both Ti_6 and

238   Ti_6_90d. The scan for Ti_6 shows the most positive strain in the y=RD direction, while strain in the

239   x=TD direction spans both positive and negative strain values (Fig. 5). A 90° sample rotation

240   (Ti_6_90d, Fig. 6) shows a 90° rotation strain, with the most positive strain values now in the x=RD

241   direction, and strain in the y=TD direction spans positive and negative values.

242   The projections of the principal strain axes are superposed as black lines onto the color maps.

243   The axis of compression (ε_1) is overlain onto the map showing the most negative deviatoric strain, and

244   the axis of extension (ε_3) is overlain onto the map showing the most positive deviatoric strain. Small

245   portions of each scan are enlarged (Figs. 5A left, 6A left) to more clearly show the relationship

246   between deviatoric strain magnitude and principal strain axis orientation.

247   For Ti_6 (Fig. 5), principal compressive strain (ε_1) show many axes displayed as dots which is

248   indicative of a large component in the z direction as the projection of the normalized principal axis

249   rotates toward the z-axis, reducing the visible length of the line to a dot. Other ε_1 axes are oriented

250   horizontally and thus dominated by a component in the x direction. The principal tensile strain (ε_3)

251   axes are mostly vertically oriented and thus parallel with the sample y-axis. The intermediate axes (ε_2)

252   are more or less aligned along the x-axis as shown by the horizontally oriented lines. For Ti_6_90d

253   (Fig. 6), the principal compressive strain axes also show a larger component in the z direction,

254   displayed by the short, dot-like projections. The principal tensile strain axes are primarily oriented

255   horizontally along the sample x-axis, and the intermediate axes are more or less vertically aligned

256   along the sample y-axis.

257   Equivalent strain has been used to estimate the magnitude of the deviatoric strain tensor (Liu,

258   2005, p. 15, eq. 1.29). For both scans, the equivalent strain was calculated to be around 3.25

259   millistrains (Fig. 7). The 90° rotated sample has some low equivalent strain values between 1 and 2

260   millistrains that are absent in the non-rotated sample. Equivalent stress maxima obtained from

261   equivalent strain using Hooke's law for Ti_6 are approximately 575 MPa. The equivalent stress for

262   Ti_6_90d shows a broader distribution with two maxima at approximately 450 and 575 MPa. These

263   fluctuations are likely due to heterogeneous stress distribution and slight variations in scan areas.

264   The orientation of principal residual strain axes $\varepsilon_1, \varepsilon_2,$ and ε_3 relative to sample coordinates

265   have been plotted as pole figures using the BEARTEX software (Wenk et al., 1998) to provide a 3D

266   visualization of the principal strain axis orientations for each scan (Fig. 8). The pole figures display

267   the 3D distributions of each strain axis in equal area projection with respect to the sample reference

268   frame. For Ti_6, a concentration of principal axes of compression is parallel to the normal direction

269   (ND), and the principal axes of extension are aligned with the rolling direction (RD). For Ti_6_90d,

270   the principal axes of compression are also oriented parallel to ND, and the principal axes of extension

271   are aligned with RD, now rotated 90°.

2.2. Deformation texture

273   The deformation texture measured in the Ti sheet is displayed with (0001) pole figures (Fig. 9A, B).

274   The crystal orientation relative to sample coordinates is determined by XMAS for each indexed

275   diffraction image based on relative peak position. Pole figures are then plotted in equal area projection

276   using BEARTEX. The experimentally determined pole figure for Ti_6 shows a girdle of maxima

277   along the transverse direction with a concentration of (0001) poles aligned close to the normal

278   direction. The pole figure for Ti_6_90d shows a 90° rotation of the girdle, still located along the

279   transverse direction which is now oriented vertically. The measured deformation textures are

280   consistent with the deformation texture of rolled Ti reduced to 3% of its original thickness (Fig. 9C)

281   (Blicharski et al., 1979).

3. Discussion

3.1. Stress and strain

284   Maps and pole figures are used to express the directionality of residual strain measured by µXRD for

285   the rolled Ti sample. The relative magnitude of the deviatoric strain tensor components (Figs. 5B, 6B)

286   suggest compression occurred in the direction normal to the sample surface (z), the normal direction

287   (ND), which agrees with the deformation conditions. The rolling direction (RD) is confirmed through

288   observation of a consistent direction of principal extension. In the non-rotated sample, this is the y-

289   axis, and in the 90° rotated sample it becomes the x-axis. Similarly, the orientation of the principal

290   strain axes show that the axis of maximum compression is parallel with the ND, and the axis of

291   maximum extension is parallel with the RD (Fig. 8).

292   These findings suggest that the residual strain measured by μXRD is consistent with the

293   deformation conditions used to produce rolled Ti. Hooke's law states a direct correlation between the

294   orientation of strain to stress, thus confirming the directionality of the principal macrostress is

295   coincident with that of the principal strains.

296   Some diffraction images could not be indexed sufficiently, likely due to high local plastic

297   strain, and thus were not used in the analysis (gray pixels in Figs. 5, 6). Plastic strain distorts the shape

298   of the reflections, and if the reflections are too highly distorted, it is difficult to accurately assign

299   Miller indices. Additionally, recrystallization, another possibility, results in many small grains and

300   thus very small diffracting volumes that produce overlapping, low intensity Laue peaks with many

301   crystallites which are difficult to index. This technique is limited to samples with large enough crystal

302   size and which have also not been severely plastically deformed. To ensure accurate analysis, a

303   minimum number of indexed peaks per diffraction pattern is necessary, and this number is dependent

304   upon the material. Quartz can have upwards of 50 peaks per diffraction pattern from an undeformed

305   sample, other materials like titanium have around 15 peaks per diffraction pattern. Approximately two

306   thirds of the expected peaks should be indexed for strong confidence in the strain measurement. If

307   indexing is less satisfactory, it is likely due to small crystallite size or high plastic deformation for

308   which alternative techniques would be more successful such as high resolution EBSD measurements

309   (Qian et al., 2017), and for samples with high amounts of plastic deformation, equations have been

310   developed to estimate the magnitude of strain based on peak shape and size (Ungár and Groma, 1989;

311   Barabash et al., 2003; Ice et al., 2004)

312   The variation in stress orientation can be attributed to grain statistics and inhomogeneous

313   stress distribution amongst the grains in the polycrystalline sample; crystal orientation, grain boundary

314   geometries, and grain-grain interactions affect how each grain experiences stress (Wilkinson &

315   Dingley, 1992) (Fig. 1). Additionally, only a small portion of the overall sample was measured during

316   this experiment and, due to the large grain size, poor grain statistics could distort the representation of

317   strain in this sample. This is likely the cause for the broadness of strain distributions around their

318   maxima (Figs. 5B, 6B and 8).

319   The equivalent stress calculations show a maximum between 400 – 600 MPa (Fig. 7). This is

320   similar in magnitude to residual stress measured in a Ti-Al-V alloy (Fig. 10 in Wang et al., 2020) and

321   low-Fe Ti alloys (Fig. 7.25 in Schajer, 2013). The broadness of equivalent strain distributions (Fig. 7),

322   and the variation in ε_{zz} distribution (Figs. 5B & 6B) could be due to slight variations in the areas

323   scanned due to the manual 90° sample rotation and thus different grains were measured. This could be

324   ameliorated with the use of fiducial markers indicating scan start and stop points. A smaller raster step

325   size would also decrease the variability in strain measured due to slight differences in the scanned area

326   between sample rotations. Additionally there will be some variation in the strain measured (Figs. 5B

327   and 6B) because the diffraction images and the optimized indexation routine are unique for each scan.

328   Indexation parameters optimized for both scans could be averaged and applied such that the treatment

329   of Laue diffraction images was identical for both scans, which could eliminate any variation in stress

330   due to slight variations in indexation caused by optimization.

331

3.2. Deformation texture

333   The (0001) pole figures for both scans are consistent with the deformation texture of rolled Ti (Fig. 9).

334   Compared to Blicharski et al. (1979), our images are more irregular which we attribute to grain

335   statistics with relatively few grains compared with pole figure goniometry, and representative of a

336   deformation texture reflective of the sample surface rather than the bulk material, as well as

337   inhomogeneous strain distribution in a polycrystalline material (Wilkinson & Dingley, 1992). The

338   deformation textures produced have been attributed to basal and pyramidal slip and twinning

339   (Zaefferer, 2003).

4. Conclusions

341   The directionality of the residual strain agrees with the deformation conditions of the rolled Ti, and

342   the magnitudes of residual strain measured are in agreement with values measured in other studies.

343   This suggests that μXRD and XtalCAMP are effective methodologies that could be used to determine

344   the directionality of residual stress reflective of the macroscopic deformation endured by crystalline

345   materials. Our new method of residual strain pole figures provides an approach for a three-

346   dimensional representation of residual strain, analogous to crystallographic pole figures in texture

347   analysis. It also concludes that our predictions of macrostress directionality for quartzite appear to be

348   reliable, thus making quartz a useful "paleopiezometer" to record geological deformation histories.

349   Future work should be done to develop the methodology for materials with different crystal

350   symmetries.

356   used Beamline 12.3.2 which is a resource of the Advanced Light Source, a U.S. DOE Office of

357   Science User Facility under contract no. DE-AC02-05CH11231.

358   **References**

359   Blicharski, M., Nourbakhsh, S. & Nutting, J. (1979). *Met. Sci.* **13**, 516–522.

360   Barabash, R.I., Ice, G.E. & Walker, F.J. (2003). *J. Appl. Phys.* **93**, 1457-1464.

361   Britton, T.B., Dunne, F.P.E. & Wilkinson, A.J. (2015). *Proc. Math. Phys. Eng.* **471**, 20140881.

362   Cauchois, R., Borbély, A., Gergaud, P., Saadaoui, M. & Inal, K. (2014). *Adv. Mat. Res.* **996**, 930-935.

363   Chen, K., Kunz, M., Li, Y., Zepeda-Alarcon, E., Sintubin, M. & Wenk, H.-R. (2016). *Geophys. Res.*

364   *Lett.* **43**, 6178–6185.

365   Chen, K., Kunz, M., Tamura, N. & Wenk, H.-R. (2011). *Eur. J. Mineral.* **23**, 169–178.

366   Dumontet, N., Connétable, D., Malard, B. & Viguier, B. (2019). *Scripta Mat.* **167**, 115-119.

367   Guo, Y., Collins, D.M., Tarleton, E., Hofmann, F., Tischler, J., Liu, W., Xu, R., Wilkinson, A.J. &

368   Britton, T.B. (2015). *Acta Mat.* **96***, 229–236.

369   Hofmann, F., Song, X., Jun, T.-S., Abbey, B., Peel, M., Daniels, J., Honkimäki, A.M., & Korsunsky,

370   A.M. (2010). *Mat. Lett.* **64**, 1302–1305.

371   Hosford, W.F. (2005). Mechanical Behaviors of Materials. United Kingdom: Cambridge University

372   Press.

373   Ice, G.E., Larson, B.C., Tischler, J.Z., Liu, W. & Yang, W. (2005). *Mat. Sci. Eng. A.* **399**, 43–48.

374   Ice, G.E., Larson, B.C., Yang, W., Budai, J.D., Tischler, J.Z., Pang, J.W.L., Barabash, R.I. & Liu, W.

375   (2004). *J. Synchrotron Rad.* **12**, 155-162.

376   Jiang, T., Wu, C., Tamura, N., Kunz, M., Kim, B.G., Son, H.-Y., Suh, M.-S. & Im, J. (2014). *IEEE*

377   *Trans. Device Mater. Reliab.* **14**, 698–703.

378   Krawitz, A.D. & Holden, T.M. (1990). *MRS Bull.* **15**, 57–64.

379   Kwon, E.P., Sato, S., Fujieda, S., Shinoda, K., Kajiwara, K., Sato, M. & Suzuki, S. (2013). *Mat. Sci.*

380   *Eng. A.* **570**, 43–50.

381   Levine, L.E., Larson, B.C., Yang, W., Kassner, M.E., Tischler, J.Z., Delos-Reyes, M.A., Fields, R.J.

382   & Liu, W. (2006) *Nat. Mater.* **5**, 619–622.

383   Li, Y. Chen, K., Dang, X., Zhang, F., Tamura, N., Ku, C.-S., Kang, H. & Wenk, H.-R. (2020). *J.*

384   *Appl. Cryst.* **53**, 1392–1403.

385   Liu, A. (2005). *Mechanics and Mechanism of Fracture: An Introduction*, Ohio, USA: ASM

386   International.

387   Lonardelli, I., Gey, N., Wenk, H.-R., Humbert, M., Vogel, S.C. & Lutterotti, L. (2007). *Acta Mat.* **55**,

388   5718–5727.

389   Lütjering, G. & Williams, J.C. (2007). *Titanium*, second ed., Heidelberg: Springer.

390   Ma, Z.S., Zhou, Y.C., Long, S.G. & Lu, C. (2012). *Surf. Coat. Technol.* **207**, 305–309.

391   Mehta, A., Gong, X.-Y., Imbeni, V., Pelton, A.R. & Ritchie, R.O. (2007). *Adv. Mater.* **19**, 1183–1186.

392   Morawiec, A. (2018). *J. Appl. Cryst.* **51**, 148–156.

393   Noyan, I.C., Bunn, J.R., Tippett, M.K., Payzant, E.A., Clausen, B. & Brown, D.W. (2020) *J. Appl.*

394   *Cryst.* **52**, 494-511.

395   Noyan, I.C & Cohen, J. B. (1987). *Residual Stress*. New York: Springer.

396   Noyan, I.C., Huang, T.C. & York, B. R. (1995). *Crit. Rev. Solid State and Mater. Sci.* **20**, 125-177.

397   Renversade, L. & Borbely, A. (2017). *J. Appl. Cryst.* **50**, 1144-1157.

398   Robinson, J.S., Truman, C.E., Pirling, T. & Panzner, T. (2017). *Mater. Sci. Forum* **905**, 31–39.

399   Schajer, G.S. (2013). *Practical Residual Stress Measurement Methods*. United Kingdom: Wiley.

400   Shen, H., Chen, K., Kou, J., Jia, Z., Tamura, N., Hua, W., Tang, W., Ehrenberg, H. & Doeff, M.

401   (2022). *Mater. Today **57**, 180-191*.

402   Spolenak, R., Brown, W.L., Tamura, N., MacDowell, A.A., Celestre, R.S., Padmore, H.A., Valek, B.,

403   Bravman, J.C., Marieb, T., Fujimoto, H., Batterman, B.W. & Patel, J.R. (2003). *Phys. Rev. Lett.* **90**,

404   096102.

405   Tamura, N. (2014). XMAS: a versatile tool for analyzing synchrotron microdiffraction data. In: G.

406   Ice, & B. Barabash, editors. *Strain dislocation gradients from diffraction*. Vol. 4. Singapore: World

407   Scientific, p. 125– 55.

408   Tamura, N., Celestre, R.S. & MacDowell, A.A. (2002). *Rev. Sci. Instrum.* **73**, 1369-1372.

409   Ungár, T. & Borbély, A. (1996). *Appl. Phys. Lett.* **69**, 3173-3175.

410   Ungár, T. & Groma, I. (1988). *J. Appl. Cryst.* **22**, 26-34.

411   Ungár, T., Gubicza, J., Ribárik, G. & Borbély, A. (2001). *J. Appl. Cryst.* **34**, 298-310.

412   Van Puymbroeck, E., Nagy, W., Schotte, K., Ul-Abdin, Z. & De Backer, H. (2019). *Appl. Sci.* **9**, 536.

413   Wang, F., Men, X., Liu, Y. & Fu, X. (2020). *Simul. Model. Pract. Theory* **104**, 102121.

414   Wenk, H.-R., Chandler, B.C., Chen, J., Li, Y., Tamura, N. & Yu, R. (2020). *Geophys. J. Int.* **222**,

415   1363–1378.

416   Wenk, H.-R., Matthies, S., Donovan, J. & Chateigner, D. (1998). *J. Appl. Cryst.* **31**, 262-269.

417   Wilkinson, A.J. & Dingley, D.J. (1992). *Acta Metall. Mater.* **40**, 3357–3368.

418   Wissink, M.L., Chen, Y., Frost, M.J., Curran, S.J., Rios, O., Sims, Z.C., Weiss, D., Stromme, E.T. &

419   An, K. (2020). *Proc. Natl. Acad. Sci. U.S.A.* **117**, 33061–33071.

420   Withers, P.J. (2007). *Reports on Progress in Physics* **70**, 2211–2264.

421   Zaefferer, S. (2003). *Mat. Sci. Eng.:A.* **344,** 20–30.